Rare Metal Materials and Engineering
Volume 52, Issue 8, August 2023
Available online at www.rmme.ac.cn

Science Press

Cite this article as: He Chaojun, Hu Ping, Xing Hairui, et al. Microstructure and Room Temperature Tensile Properties of Rolled Mo-14%Re Alloy[J]. Rare Metal Materials and Engineering, 2023, 52(08): 2746-2756.

ARTICLE

Microstructure and Room Temperature Tensile Properties of Rolled Mo-14%Re Alloy

He Chaojun[1,2], Hu Ping[1,2], Xing Hairui[1,2], Yang Fan[1,2], Zhang Xiangyang[1,2], Lin Xiaohui[3], Hua Xingjiang[1,2], Bai Run[3], Zhang Wen[3], Wang Kuaishe[1,2]

[1] School of Metallurgy Engineering, Xi'an University of Architecture and Technology, Xi'an 710055, China; [2] National and Local Joint Engineering Research Center for Functional Materials Processing, Xi'an University of Architecture and Technology, Xi'an 710055, China; [3] Northwest Institute for Nonferrous Metal Research, Xi'an 710016, China

Abstract: Mo-Re alloys have excellent mechanical and processing properties due to their high-temperature resistance, corrosion resistance, and plasticity. To further understand the microstructure and room temperature tensile properties of rolled Mo-14%Re alloy, the microstructure and fracture morphology of the Mo-14%Re alloy were investigated by scanning electron microscopy (SEM) and high-resolution electron backscatter diffraction (EBSD). Channel 5 software was used to analyze the microstructure evolution of rolled Mo-14%Re alloy at different annealing temperatures. With the increase in annealing temperature, the Schmidt factor of the Mo matrix phase and ReO_3 phase decreases gradually. The texture intensity increases rapidly, and the crystal orientation intensity of the polarography increases from 6.51 to 10.18. The initial recrystallization of the rolled Mo-14%Re alloy occurs at 1100 °C, at which the uniform precipitation of the earth-rich ReO_3 phase in the alloy leads to uniform stress distribution during tensile process, the grains of Mo matrix phase and ReO_3 phase show obvious ＜101＞ crystal orientation and ＜111＞ crystal orientation, and the grain boundaries of ReO_3 phase are mainly high-angle grain boundaries, which makes the elongation after fracture reach the maximum of 33.5%. The tensile fracture has the highest number of dimples and the largest size. Besides, the formation, aggregation, growth, and crack propagation of micropores during fracture were studied.

Key words: Mo-14%Re alloy; room temperature tension; initial recrystallization; microstructure evolution; crack extension

Molybdenum (Mo) is a rare refractory metal with excellent physicochemical and mechanical properties[1–3]. Rhenium (Re) is a rare precious metal that is widely used in aerospace[4–5], medicine, and catalysts[6] because of the high corrosion resistance, high-temperature resistance, excellent electronic structure and catalytic activity. Different from pure molybdenum, molybdenum-rhenium (Mo-Re) alloys have very high work hardening rates. Because of the high melting point, high strength, high hardness, good plasticity, good thermal conductivity, and electrical conductivity, Mo-Re alloys possess high-temperature resistance, corrosion resistance, and good mechanical and processing properties. Que et al's study[7] showed that the stress factor and hardening index increase with raising the Re content, but the stress factor of Mo-Re alloys is much smaller than that of pure Re, indicating that the work hardening probability of Mo-Re alloys is much smaller than that of pure Re, and the element Re can change the anisotropy of Mo alloys[8]. With the increase in Re content, the elastic constants in the (100) direction decrease, while the elastic constants in the (110) and (111) directions increase. When the mass fraction of Re is 50wt%, Mo-Re alloys exhibit isotropic properties with the same elastic constants in different directions[9].

Molybdenum (Mo) has received extensive attention as a very promising refractory metal material[10]. TZM molybdenum alloy has broad application prospects in aerospace, high temperature heating devices and other fields due to its

Received date: February 28, 2023
Foundation item: National Key R&D Program of China (2022YFB3705400); Major Scientific and Technological Projects in Shaanxi Province of China (2020ZDZX04-02-01); Scientific and Technological Innovation Team Project of Shaanxi Innovation Capability Support Plan of China (2022TD-30); the Fok Ying Tung Education Foundation (171101); Youth Innovation Team of Shaanxi Universities (2019-2022); Top Young Talents Project of "Special Support Program for High level Talents" in Shaanxi Province (2018-2023); China Postdoctoral Science Foundation (2021M693878); Service Local Special Program of Education Department of Shaanxi Province, China (21JC016); Key R&D Program of Shaanxi Province, China (2021GY-209)
Corresponding author: Hu Ping, Ph. D., School of Metallurgy Engineering, Xi'an University of Architecture and Technology, Xi'an 710055, P. R. China, E-mail: huping@xauat.edu.cn

easiness of processing and excellent performance[11]. However, its application and processing performance are limited due to its weak structural characteristics and poor high temperature oxidation resistance[12]. A small number of rare earth oxides can significantly improve the concave resistance and high-temperature tensile property of pure Mo. Mo alloy doped with rare earth element La has high strength, high recrystallization temperature, and a low ductile-to-brittle transition temperature (DBTT)[13]. The effect of Re on the properties of Mo has been extensively studied. The plasticity of Mo at room temperature is limited, while adding 26.4at% (41wt%) or 31.8at% (47.5wt%) Re or other rare earth elements can reduce the transition temperature from ductile to brittle[14]. However, the ultimate tensile strength (UTS) of Mo-31.8at% Re at 1700 K and 160 MPa is significantly lower than that of Re at 300 MPa[15]. Re can form $MoReO_4$-type compounds with Mo, which are different from MO_2-type compounds without grain boundary penetration. The solid solution of Re in Mo forms the α-phase with a body-centered cubic structure, and the maximum solubility is 59% at 2500 °C. With the decrease in temperature, the solubility is only 29% at room temperature, and the solid solution of Mo forms a dense hexagonal β phase[7]. Re can increase the recrystallization temperature of Mo alloy and weaken the anisotropy of Mo[8, 16]. Mo-Re alloy has good mechanical and processing properties.

Mo-Re alloys are generally prepared by the powder metallurgy or vacuum melting method. The vacuum melting method can control the impurity content of Mo-Re alloy ingots. The decrease in the gas element content is beneficial to the subsequent processing of Mo-Re alloy[17]. The oxidation roasting process effectively separates the oxidation products MoO_3 and Re_2O_7[17]. The vapor pressure of MoO_3 is much lower than that of Re_2O_7 (0.0067 kPa at 650 °C, 0.028 kPa at 670 °C, and 0.059 kPa at 700 °C)[17], and minimal amounts of MoO_3 volatilize at high temperatures[18], resulting in the loss of Mo. Notably, the low-valence Re oxide ReO_3 is nonvolatile due to its external vapor pressure (only 0.013 kPa at 400 °C)[17]. Liu et al[19] used wet mixing or dry-wet mixing to facilitate the uniform distribution of Re. The Mo-3Re alloys prepared by the dry-wet mixing method have higher tensile strength and recrystallization onset temperature than Mo-3Re alloys prepared by the mixing method. Compared with the pendant melting method, Mo-Re alloy prepared by the dry hydrogen sintering method has a fine grain structure, high tensile strength, elongation, and microhardness[20]. Han et al[21] achieved the development of Mo-41Re and Mo-45Re alloys in narrow strips for the first time and studied the related properties in detail. Subsequently, the development of Mo-41Re alloy for traveling wave tube deletion network and studies such as cross-rolling and cup-convex experiments were conducted for stamping and forming[22]. It is necessary to pay attention to the influence of oxygen on the alloy during the preparation and processing. The plasticity of Mo-13Re alloy with low Re content is poorer than that of Mo-Re alloy with Re content less than 13%, mainly due to the high oxygen content in Mo-13Re alloys[23]. Mannheim et al[24] conducted an accurate determination for the phase structure of Mo-Re alloys prepared by powder metallurgy. Garin[25] studied the constant lattice variation and phase structure of Mo-Re alloys sintered at medium temperature with Re content up to 87% using the XRD method.

Although the study of Mo-Re alloys is gradually progressing, there are still problems in controlling the content of elements in Mo-Re alloys. It is necessary to study the high-temperature aging properties of Mo-Re alloys[26]. Previous research focuses on the small size of Mo-Re alloys, and the study on the application performance of Mo-Re alloys is less. Therefore, the research on related fields is still insufficient, and there are certain limitations. Mo-Re alloys with high Re content have been studied, but some gaps still exist in studying similar mechanisms for Mo-Re alloys with low Re content. In this study, the tensile properties and microstructure of rolled Mo-14%Re alloy tubes annealed at 900, 1100, and 1300 °C were analyzed by energy spectrum analysis (EDS), scanning electron microscopy (SEM), high-resolution electron backscatter diffraction (EBSD) techniques and data processing software. Effect of annealing on microstructure evolution of rolled Mo-14% Re alloy tube was studied, and the micropore formation, aggregation, growth, and crack propagation during fracture were analyzed.

1 Experiment

1.1 Experimental materials

The Mo-14%Re was prepared by powder metallurgy process in this study. The Mo powder and Re powder were mixed, cold isotactic forming was conducted at 150 MPa for 2 min, high-temperature hydrogen sintering was used to obtain sintered billet, and then high temperature forging and rotary forging were applied at 1450 and 1200 °C, followed by polishing to get deformation rate higher than 82% of the bar. The bar was machined to obtain a tube billet. Then hot rolling was carried out to obtain the tube, followed by straightening and alkali washing and heat treatment. Fig.1 is the preliminary process of the Mo-14%Re tube.

1.2 Tensile tests and microstructure characterization

The rolled and annealed at 900, 1100, and 1300 °C for 1 h in a vacuum annealing furnace (1×10^{-3} Pa) Mo-14%Re tube tensile samples were named as O-1, O-2, O-3, and O-4, respectively. Vickers hardness for annealed samples was measured by 401MVD testing machine. A certain size of sample was cut from the tensile sample. The surfaces were polished with different grit sandpapers and then polished with 1.5 μm alumina for energy dispersive spectroscopy (EDS) characterization. Gemini SEM 300 scanning electron microscope (SEM) was used to observe the microstructure. Electron backscatter diffraction (EBSD) was selected to characterize the microstructure. Low-angle grain boundaries (LAGBs, 2°–15°) and high-angle grain boundaries (HAGBs, > 15°) were identified by strip contrast and grain boundary map. Fig. 2 shows the EBSD sampling position, and the cross-section of the specimen was selected to investigate the

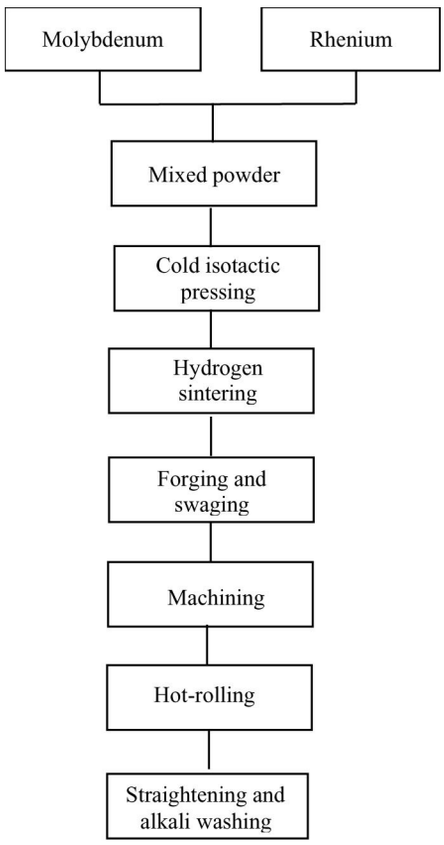

Fig.1 Processing flow of the Mo-14%Re tube

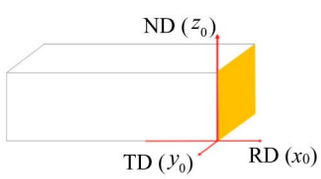

Fig.2 Sampling position for EBSD test

relationship between microstructure and grain orientation. The tensile properties of O-1, O-2, O-3, and O-4 samples were tested by the Instron 8801 testing machine at room temperature according to GB/T 228.1-2010. Fig. 3a is the geometric parameters of the tensile specimen in this test. Finally, the yield strength (YS), ultimate tensile strength (UTS), and elongation after the break were obtained by engineering strain stress. Fig. 3b shows the fracture sample after the tensile test.

2 Results and Discussion

2.1 Microstructure characterization of rolled Mo-14%Re by SEM

Fig. 4 is the microstructures of O-1, O-2, O-3, and O-4 samples. The initial recrystallization temperature of the rolled Mo-14% Re alloy is 1100 °C. The grain length-diameter ratio has an unavoidable shrinkage and widening tendency with increasing annealing temperature. For O-4 sample, when the temperature rises to 1300 ° C, the microstructure of the tube is

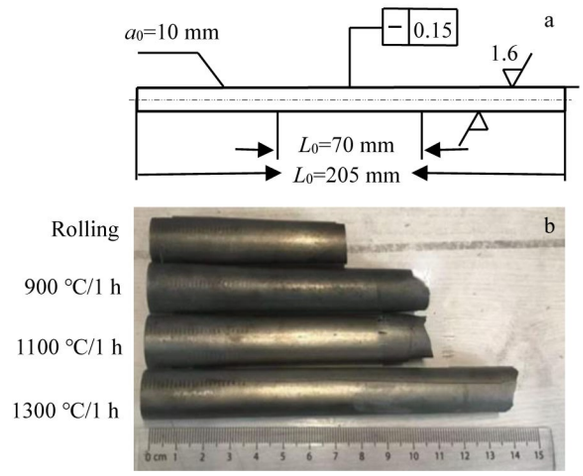

Fig.3 Geometric dimensions of the tensile (a) and fracture (b) samples

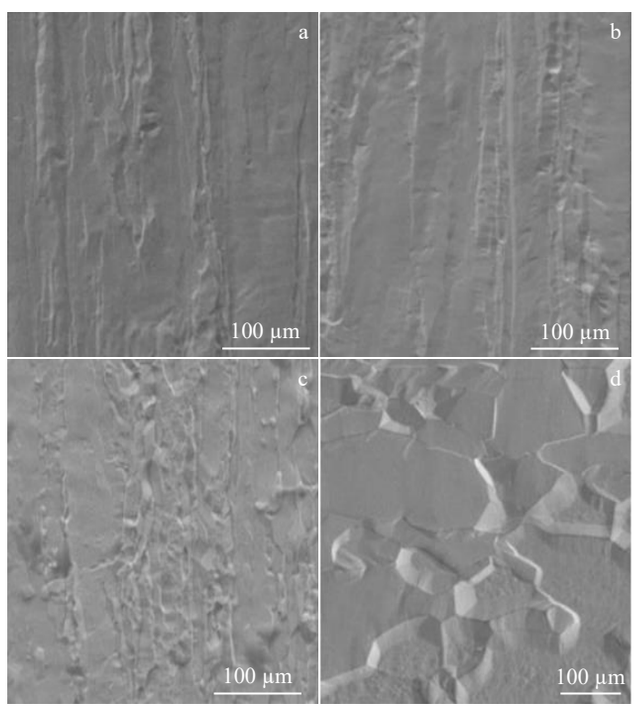

Fig.4 SEM microstructures of O-1 (a), O-2 (b), O-3 (c) and O-4 (d) samples

still fine, and the grain and fiber structure are elongated. For O-3 sample, compared with Fig.4a and 4b, the central part of the microstructure is still delicate fibrous structure. The lateral distance of the fibrous structure outside the central part is widened, and the fibrous widening phenomenon occurs from the center to the periphery. And it is accompanied by sporadic small-sized equiaxed grains, the number of fine grains increases greatly and is gradually evenly distributed, indicating that recrystallization begins to appear at this stage. The recrystallized grains in O-4 sample grow further, resulting in larger grain size and a particular weakening effect at a higher temperature.

2.2 EBSD characterization of rolled Mo-14%Re

In order to analyze the whole annealing process of four samples, a detailed microstructure analysis was carried out. EBSD was used to investigate the phase distribution at the interface, as shown in Fig. 5. The Mo-based solid solution is marked by red, and the resulting ReO_3 phase is marked as green because of metallurgical action. Fig. 5a shows the random distribution of the green ReO_3 phase at the interface, and after annealing treatment, compared with Fig.5a, the ReO_3 step in Fig. 5b tends to migrate toward the grain boundaries gradually. At the initial recrystallization temperature, the volume fraction content of ReO_3 phase is the lowest. Molybdenum-rhenium alloy is a solid solution alloy. Rhenium forms a β solid solution in molybdenum. In the Mo-14%Re alloy, the O atom penetrates the surface layer and gradually diffuses into the interior of the alloy; after reaching the interior of the alloy, it diffuses into dislocations and other defects inside the alloy. Part of Re is dissolved into the matrix Mo, and the rest is enriched at the grain boundary and combined with oxygen to form ReO_3. Annealing at recrystallization temperature further promotes more rhenium to dissolve into the molybdenum matrix, making its oxide content lower. The ReO_3 phase is mainly distributed at grain boundaries, which can promote the microstructure uniformity in Fig. 5c. The average grain size of the oxide particles in the O-1, O-2, O-4 samples is 5−8 μm, and that in the O-3 sample is 2−3 μm. The formation of coarser oxides and agglomerates increases the grain size of the alloy. On the contrary, the finer the grains, the more the grain boundaries and the greater the resistance to dislocation movement, and thus the plastic deformation resistance of the metal increases. At the same time, as the the number of grains increases, the plastic deformation of the metal can be dispersed into more grains, and the grain boundary will also prevent the expansion of cracks, so that the mechanical properties of the sample O-3 are improved. It is also noted that there are also significant differences in the morphology of oxides in the four samples. In the interface matrix of O-3 sample, a large number of near-spherical oxides are evenly distributed around the slender ReO_3. The near-spherical structure has a good plasticity and toughness, and its comprehensive mechanical properties are better. It is not easy to crack during cold deformation. In comparison, O-1, O-2, O-4 samples have a variety of oxide morphologies, and the stacking and aggregation of oxides are obvious, resulting in stress concentration and producing various defects such as microcracks, voids, which makes the overall mechanical properties of the alloy decrease. The rare earth-rich ReO_3 phase precipitates uniformly at grain boundaries at the interface, which realizes the uniform charge distribution[27] and inhibits metal transformation to covalent bonds[28]. Table 1 shows the maximum elongation of 33.5%. With a higher annealing temperature, the stronger the atomic diffusion ability, the easier the grain boundaries to migrate, and the faster the grain growth, which leads to the rapid grain growth of the ReO_3 phase in Fig.5d.

Channel 5 software was used to further explore the microstructure evolution of rolled Mo-14%Re during annealing. Fig. 6 shows the Schmid factor distribution of the phase composition of the four alloys. Particles of different colors represent different Schmid factor values. The depth of red represents the value of the Schmid factor. It can be found that the Schmid factor of Mo matrix phase and ReO_3 phase

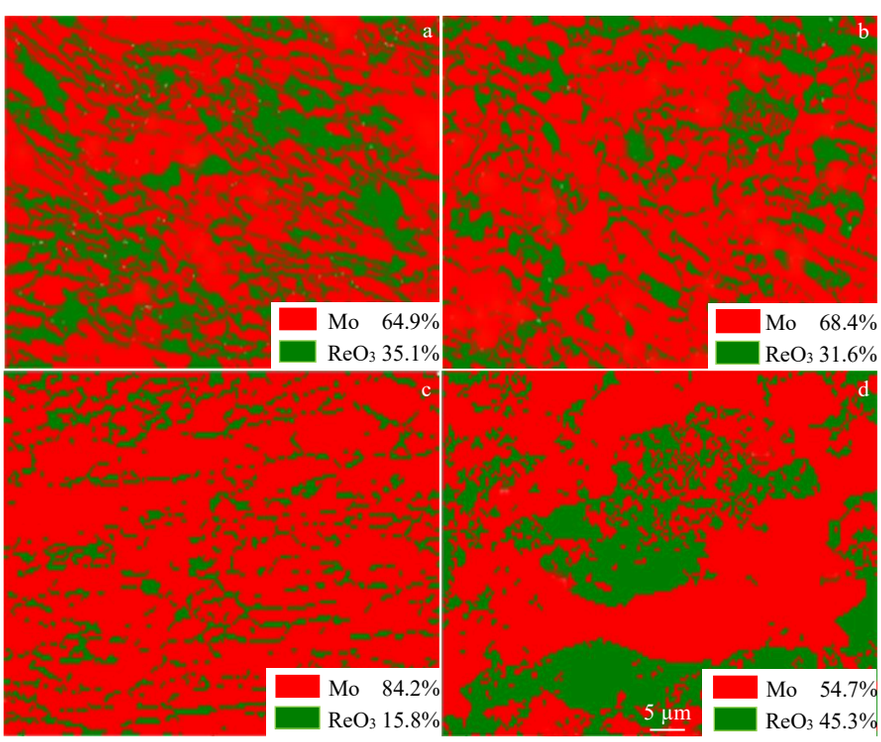

Fig.5 Phase distribution at the interfaces of O-1 (a), O-2 (b), O-3 (c) and O-4 (d) samples

Table 1 Room temperature tensile properties of Mo-14%Re sample

Sample	R_m/MPa	$R_{p0.2}$/MPa	A/%
O-1	826	681	26.5
O-2	763	649	28.5
O-3	720	511	33.5
O-4	598	372	28.0

components is the largest in Fig. 6a. With the increase in annealing temperature, the Schmid factor of the Mo matrix phase and ReO_3 phase in Fig.6b–6d gradually decreases.

Fig. 7 shows the distribution of misorientation angle. Compared with sample O-1, with the increase in annealing temperature, the average misorientation angle of the Mo matrix phase and the proportion of high angle grain boundary gradually increase. At the same time, the grain boundaries of the ReO_3 degree in Fig.7b and 7c are mainly high angle grain boundaries, while the grain boundaries of the ReO_3 phase in Fig. 7a and 7d are low angle grain boundaries. Low angle grain boundaries ReO_3 grain are more than 45.7%, and account for most of the whole grains in Fig.7a of sample O-1.

The anisotropy of the mechanical properties is related to the orientation of merit in internal structures. The concentration and uniform distribution of grain orientation have a significant effect on the properties of materials. Fig. 8 gives the grain

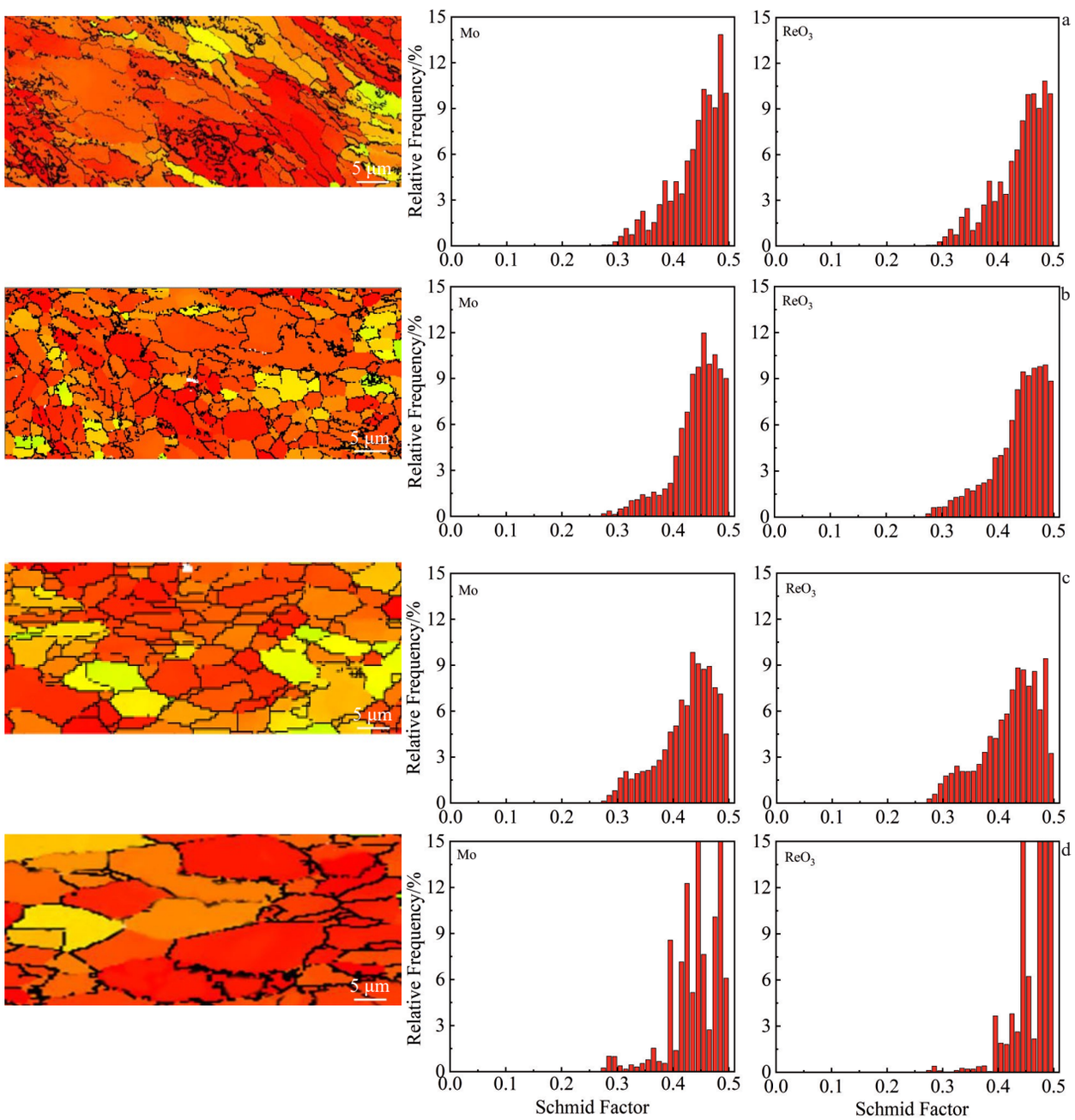

Fig.6 Schmid factor distribution of phase composition of O-1 (a), O-2 (b), O-3 (c) and O-4 (d) samples

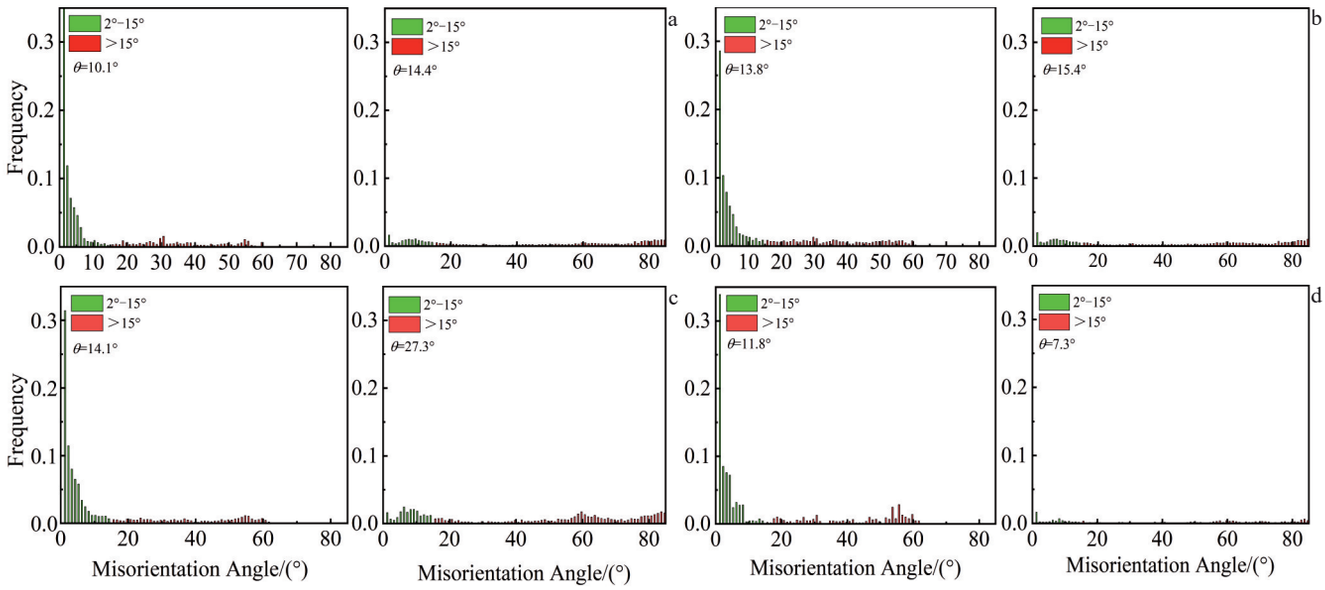

Fig.7 Misorientation angle distribution of O-1 (a), O-2 (b), O-3 (c) and O-4 (d) samples

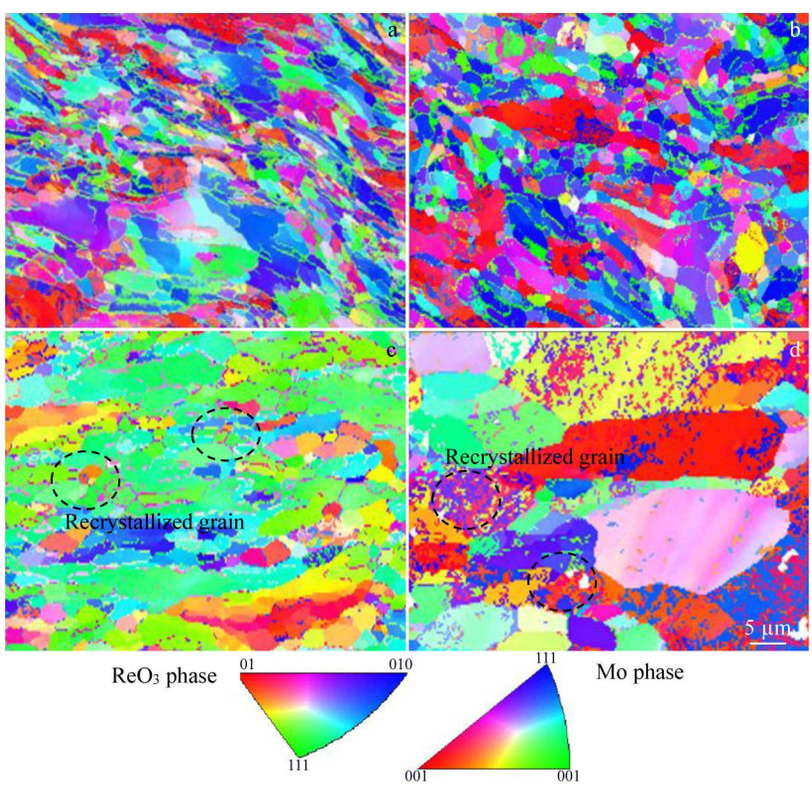

Fig.8 Grain orientation diagram of O-1 (a), O-2 (b), O-3 (c) and O-4 (d) samples

orientation diagram. As shown in Fig. 8c and 8d, there are some recrystallized grains (marked by circles), indicating that the grains can be nucleated at the normal boundary at this temperature. With the change of rolling state and three different annealing temperatures, the two-phase grains of the Mo matrix phase and ReO_3 phase in Fig. 8c show more obvious <101> crystal orientation and <111> crystal orientation. In contrast, the two-phase grains of Mo matrix phase and ReO_3 phase mainly show <111> crystal orientation and <010> crystal orientation in Fig.8a, 8b and 8d.

Fig. 9 shows the pole figures of O-1, O-2, O-3, and O-4 samples, where Fig. 9b–9d indicate that with the increase in annealing temperature, the crystal orientation strength parallel to the direction increases. There is a rapid increase in texture intensity, in which the power of crystal orientations increases from 6.51 to 10.18 in the pole figure. The distribution is more

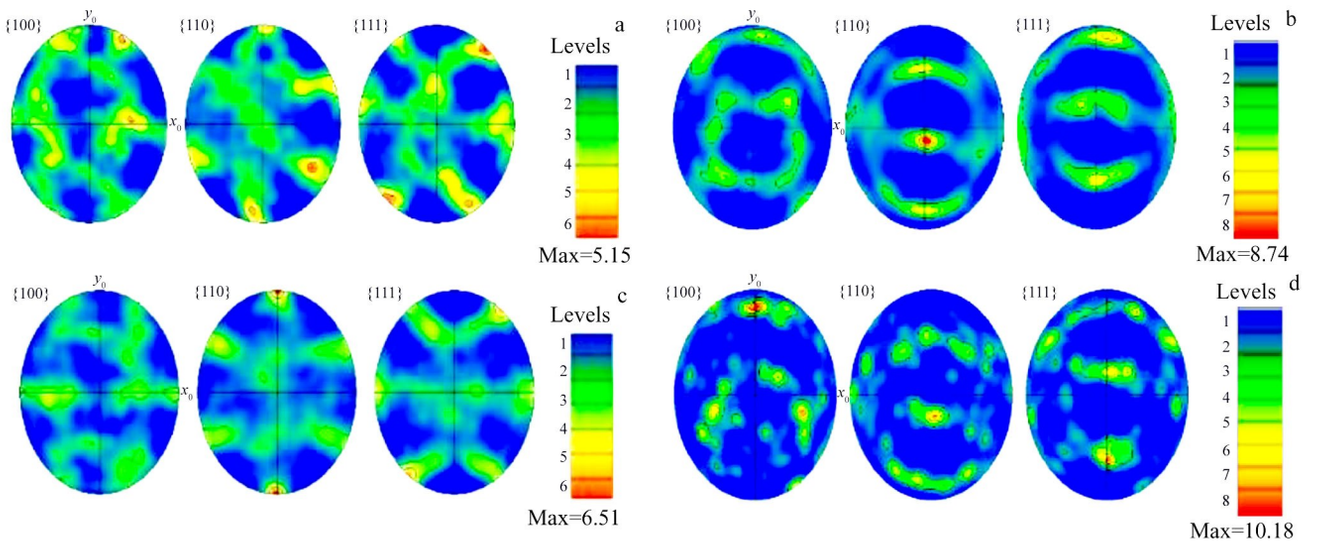

Fig.9 Pole figures of O-1 (a), O-2 (b), O-3 (c), and O-4 (d) samples

scattered and not concentrated in the center of the pole figure. The basal texture {100} is strengthened, and the {110} and {111} textures are strengthened as the annealing temperature increases, so the maximum intensity is almost concentrated in the {110} and {111} pole figures. In Fig. 9c and 9d, the migration between the original coarse grain and the newly formed small grain[29] is small, and the grain orientation distribution is irregular.

Driven by stored deformation energy, recrystallization grain develops into a new grain structure through nucleation and movement of large-angle grain boundary[30]. To study the variation of recrystallization during the deformation process in detail, Fig. 10 shows the distribution and volume fraction of recrystallization grain after heat treatment. After annealing at 1100 °C, the volume fraction of recrystallized grains is about 56.9%, and the deformed grains at grain boundary account for 25.1%. The broken grains appear as smaller recrystallized grains at grain boundaries. The recrystallization process exerts a large amount of energy in the plastic deformation process. Due to many defects, energy storage is released as the

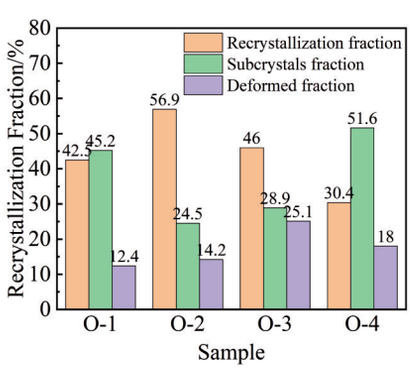

Fig.10 Recrystallization distribution and volume fraction of O-1, O-2, O-3 and O-4 samples

nucleation driving force, which reduces the recrystallization temperature and promotes the nucleation rate. The number of sub-grains and recrystallized grains of rolled Mo-14%Re increases after annealing.

2.3 Tensile properties of rolled Mo-14%Re

In the tensile test at room temperature, the changes in tensile strength R_m, yield strength $R_{p0.2}$, and elongation A of the rolled Mo-14%Re are shown in Table 1. With the increase in annealing temperature, the high-temperature weakening phenomenon leads to a decrease in strength and increase in plasticity. The tensile strength R_m of O-1 sample is 826 MPa, the yield strength is 681 MPa, and the elongation A after fracture is only 26.5%. After three times of heat treatment, the minimum tensile strength R_m of the tube is 598 MPa, the minimum yield strength is 372 MPa, and the maximum elongation to fracture is 33.5% for sample O-3. The elastic deformation energy stored in the recovery stage is high, and the dislocation density is high. The decrease in elastic deformation energy is the driving force of recovery recrystallization. The sample O-3 has the highest elongation to fracture. The earth-rich ReO_3 phase uniformly precipitates at the grain boundary as shown in Fig.4c, which leads to the promotion of stress relaxation and cohesive force of GBs, and the uniform stress distribution in the tensile process is realized. In addition, in the grain orientation shown in Fig. 8, the two-phase grains of Mo matrix phase and ReO_3 phase of sample O-3 present obvious <101> and <111> crystal orientations, while the two-phase grains of Mo matrix phase and ReO_3 phase of O-1, O-2 and O-4 samples present mainly <111> and <010> crystal orientations. In comparison, the plasticity of O-2 and O-3 samples is relatively high. The main reason for Fig. 7 is that the grain boundaries of ReO_3 phase are mainly high-angle grain boundaries in O-2 and O-3 sample, while the grain boundaries in O-1 and O-4 samples are mainly low-angle grain boundaries. The high-angle grain boundaries make crack propagation difficult and improve the toughness of the

material. The low-angle grain boundaries make the crack easy to deflect and then to propagate along the next grain boundary, and thus the toughness decreases.

Fig.11 shows the tensile strength R_m, yield strength $R_{p0.2}$ and Vickers hardness of the rolled Mo-14%Re. Recrystallization of the deformed metal significantly reduces the strength and hardness of the metal, and the plasticity and toughness are greatly improved, which eliminates the work hardening phenomenon. With the increase in annealing temperature, the overall hardness of the rolled Mo-14%Re decreases. The hardness of the original sample is decreased by 923.16 MPa, which is 27% lower than that of the original example. The hardness of the sample decreases to 255.5×9.8 MPa in the sample O-4. This is because energy provided at the beginning of recrystal-lization is less, the recrystallization degree is slow, and the hardness decreases slowly. With the continuous increase in annealing temperature, the recrystallization rate increases, and the hardness of the alloy decreases rapidly. The hardness decline curve is consistent with the strength decline curve.

2.4 Fracture morphology of rolled Mo-14%Re

Fig. 12 shows many destructive cracks and failure surfaces in the fracture. The damaging cracks form the failure zone through the large-angle grain boundary. The general direction of crack propagation and the crack on the dematerialization surface propagate to the free surface, so that the fracture of sample O-1 exhibits a river pattern similar to cleavage characteristics, and the uneven distribution of cracks on the fiber surface is more obvious. The uneven distribution of cracks on the fiber surface becomes more apparent[31]. In Fig. 12a, the SEM fracture morphology of sample O-1 has a certain number of tearing ribs and side-off surfaces. For the rolled Mo-14%Re, when the Re content is more than 10%, the solid solution strengthening increases with the increase in Re content. At the same time, the grain size becomes more nuanced, the yield strength and tensile strength of the alloy gradually increase, the stress factor and hardening index increase, and the work hardening gradually intensifies[32]. It shows that the fracture of the Mo-Re solid solution has noticeable tearing marks. Three kinds of heat-treated samples

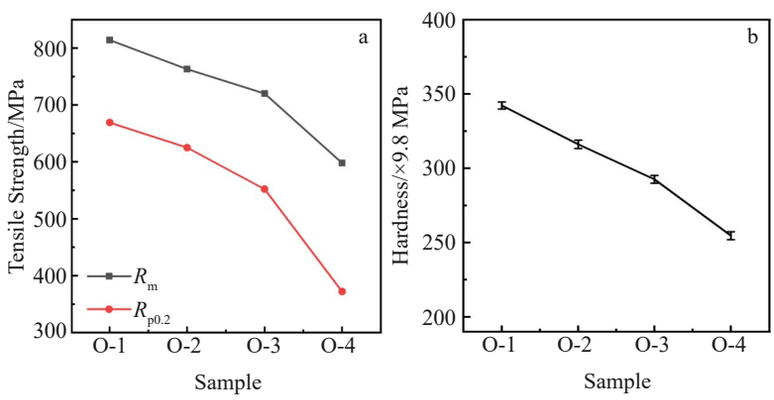

Fig.11 Mechanical properties at room temperature of Mo-14%Re: (a) tensile property and (b) Vickers hardness

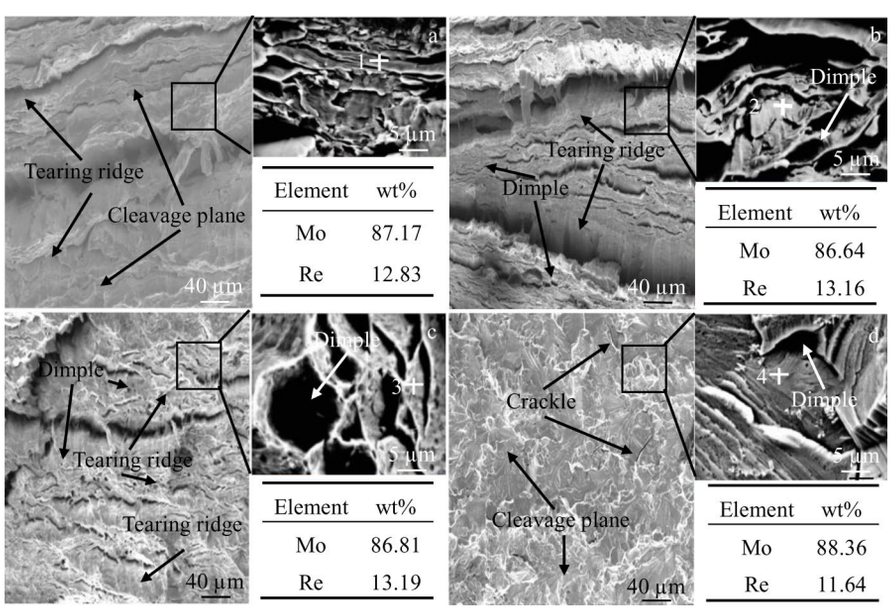

Fig.12 Fracture morphologies and element Mo and Re contents of O-1 (a), O-2 (b), O-3 (c), and O-4 (d) samples

show neck shrinkage after tensile at room temperature in Fig. 3, and there is apparent macroscopic plastic deformation. At the same time, evident transverse streamline structure of fracture appears after heat treatment, as shown in Fig. 12b – 12d. There are microscopically tear edges and dimples left after tension on the fracture surface, and the concave and convex fluctuation of the fracture surface is pronounced. It is accompanied by the existence of part of the dissociation surface, indicating that it is a mixed feature of cleavage fracture and ductile fracture. In Fig. 12b and 12c, after the tensile test, with the increase in annealing temperature, the dimple size gradually becomes more significant and more profound, and the number gradually increases. In addition, the neck deformation degree around the fracture also increases with the increase in annealing temperature. Due to the recrystallization grains, it further grows at this annealing temperature in Fig. 12d. The plasticity and microstructure change, resulting in a small number of dimples and small size at the fracture interface. After annealing treatment, the fracture surface is uneven, and the crack propagation path is very tortuous, which increases the crack propagation resistance and the energy consumption in the fracture process of the alloy. The streamlined structure formed by rolling is the coexistence of grains, which makes the alloy have a strong bonding force. Therefore, the sensitivity to cracks is effectively reduced, thereby improving the plasticity of the material.

2.5 Mechanism of micropore forming and crack extension in rolled Mo-14%Re

The classical Schmid law points out that the shear stress acting on the slip surface along the slip direction determines the slip ability of the crystal. This theory believes that the critical resolved shear stress (CRSS) must be reached, if a given slip system is activated in a deformed crystal. Schmid's law is in accordance with the choice of most sliding systems[33]. Fig. 13 is the diagram of slip systems, where F is the tensile force, φ is the angle between the tensile strength and the average line n on the slip surface, and λ is the angle between the tensile strength and the slip direction b. In the figure, the shear stress on the slip surface along the slip direction is:

$$\tau=(F/A_0)\cos\lambda\cos\varphi \quad (1)$$

$$\sigma=m\tau \quad (2)$$

where $m=1/(\cos\lambda\cos\varphi)$ is called the Schmitt factor. When the tangential stress on the slip surface reaches the critical value, the crystal begins to slip. The acute tangential stress is a material constant and has nothing to do with the crystal orientation.

$$\sigma_s=m\tau_c \quad (3)$$

The minimum value of Schmid factor is 2. The orientation factor has a maximum weight of 0.5 when $\lambda=\varphi=45°$, and the larger the value of the Schmid factor, the more likely the slip system occurs. The initiation of the alloy slip system is related to the structure, deformation mode, and stress direction of the material.

The microporous shear principle can explain the plastic fracture behavior of rolled Mo-14%Re. Oxygen molecules diffuse to the surface of Mo-14%Re alloy and partially adsorb on the alloy surface, as shown in Fig. 14a. The matrix Mo attracts the adsorbed O_2, dissociates some weak bond molecules to form a single atom, and is strongly adsorbed on the alloy surface, as shown in Fig. 14b and Eq. (4). Due to different chemical potentials of Mo and O, to reduce the system free energy, O atoms penetrate the surface layer of Mo-14%Re and gradually diffuse into the alloy, as shown in Fig. 14c. When O atoms reach the interior the alloy, they diffuse to the grain boundaries, dislocations, and other defects. Partial Re solid solution enters the Mo matrix. The rest are enriched in the grain boundary and combine with oxygen to form ReO_3, while H_2 and O escape from the interface crack of the Mo matrix, form micropores and combine to form water vapor, as shown in Fig. 14d and Eq. (5) and Eq. (6). The micro-cracks generated during the plastic deformation of the rolled Mo-14%Re alloy are the main characteristics of ductile fracture: the growth and aggregation of micro-pores until the final rupture of the specimen. After moving, the tensile sample of Mo-14%Re alloy is subjected to a particular load, and the necking phenomenon occurs, as shown in Fig. 3b above. The plastic deformation of the material increases, resulting in changes in the morphology of the pores, as shown in Fig. 14e. Under the three-dimensional tensile stress, in the middle of the room temperature tensile specimen, the micropores grow and aggregate to form cracks, as shown in Fig. 14f. The stress concentration at the crack tip makes the plastic deformation mainly concentrate at the crack tip, which makes the local

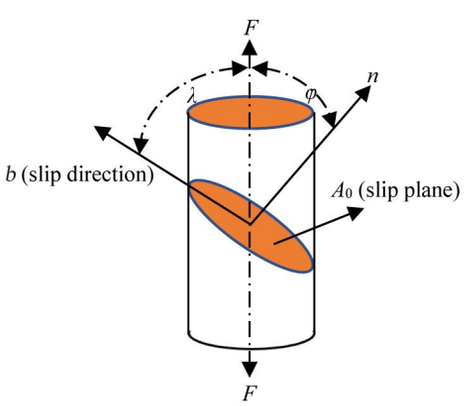

Fig.13 Distribution of the slip system

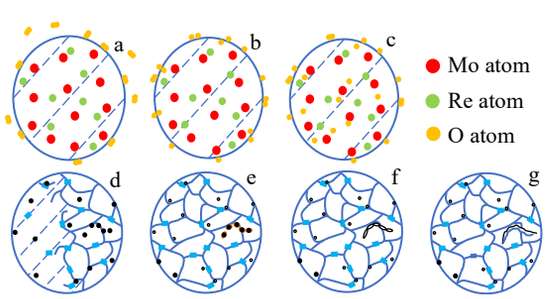

Fig.14 Fracture mechanism diagram of Mo-14%Re

plastic deformation of the material serious and forms a large number of micropores, as shown in Fig.14g. At the same time, the significant cracks also gradually develop along these micropores. The plastic constraint gradually disappears when the shot is close to the specimen surface. The crack propagates along the direction of the maximum shear stress, resulting in sheer damage and forming a ductile fracture process.

$$O_2 \rightarrow 2O \tag{4}$$

$$3O+Re \rightarrow ReO_3 \tag{5}$$

$$O+H_2 \rightarrow H_2O \tag{6}$$

In Fig. 14d, many micropores appear at the tube interface. To further explain the influencing mechanism of micropores on crack formation, various micropore growth and aggregation models were proposed based on the classical works of Zhong[31], Yuan[34], and Bridgman[35]. Under ideal conditions, assuming that the radius of the adjacent two holes and the distance between the center holes are a and b, the transverse stress component imposed by the far-field during the growth of the holes in Fig.14e is σ_{11}^{∞} and σ_{22}^{∞}, respectively. The equivalent flow strain increment is d$\bar{\varepsilon}$. This model considers the aggregating tendency of micro-pores when the micro-pore radius increases to a=b/2. When Mo-14%Re alloy has viscous rheological properties, its strain hardening relationship can be expressed as:

$$\bar{\sigma} = \sigma_0 \bar{\varepsilon}^n \tag{7}$$

where n is the strain hardening index of the material. The rate of change of the short radius of two adjacent micropores is:

$$\frac{\mathrm{d}[\ln(a/1)]}{\mathrm{d}\bar{\varepsilon}^{\infty}} = \frac{\sinh[(1-n)(\sigma_{11}^{\infty}+\sigma_{22}^{\infty})/(2\bar{\sigma}/\sqrt{3})]}{1-n} \tag{8}$$

Under certain proportional loading conditions, integrating the above equation obtains the expression of fracture strain:

$$\bar{\varepsilon}^{\infty} = \frac{(1-n)\ln(l_0/a_0)}{\sinh[(1-n)(\sigma_{11}^{\infty}+\sigma_{22}^{\infty})/(2\bar{\sigma}/\sqrt{3})]} \tag{9}$$

Among them, the strain hardening index n of the material influences the growth rate of microporosity and fracture plasticity. The Mo-14%Re metal structure under cyclic loading causes fatigue strength reduction for various reasons (e. g., stress concentration), and microporous aggregation in Fig. 14g forms initial cracks, which eventually lead to structural failure by crack expansion. Paris et al[36] presented the fundamental theorem of crack addition based on fatigue mechanics. In tube crack extension, the modified Forman's equation calculates the crack extension rate:

$$\frac{\mathrm{d}C}{\mathrm{d}N} = \frac{C_0(1-f)^{n_0}\Delta K^{n_0}\left(1-\frac{\Delta K_{\mathrm{th}}}{\Delta K}\right)^{p_0}}{(1-R)^{n_0}\left(1-\frac{\Delta K}{(1-R)K_{\mathrm{c}}}\right)^{q_0}} \tag{10}$$

$$K_{\mathrm{c}} = K_{\mathrm{IC}}(1+B_{\mathrm{K}}\mathrm{e}^{-\omega});\ \omega = \left(\frac{2hA_{\mathrm{K}}}{h_0}\right)^2;\ h_0 = 2.5\frac{K_{\mathrm{IC}}}{S_{\mathrm{Y}}} \tag{11}$$

Get these parameters from NASGRO 2.0[37], where C is the crack length, dC/dN is the increment of the crack length per cycle, ΔK_{th} is the range of the threshold stress intensity factor, K_{c} is the critical stress intensity factor, and K_{IC} is the plane strain fracture toughness. B_{K} and A_{K} are the fitting parameters, h is half of the tube thickness, h_0 is the minimum thickness required to ensure plane strain, and S_{Y} is the yield stress. Newman[38] defined the opening function f for plasticity-induced crack closure. Tanaka et al[39] derived the threshold value for the range of stress intensity factors. The equation used to predict fatigue crack extension is as follows:

$$\Delta C_j = C_0 + \Sigma_{j=1}^{i}\Delta C_j \tag{12}$$

where C_0 is the initial crack length and ΔC_{j} is the crack length increment of the jth step of the loading. Since the stress intensity factor K changes during cyclic loading, its loading history and amplitude have some influence. ΔC_{j} is set to a small value of 1. Eq. (10) calculated the crack propagation increment at the crack center and obtained the following equation:

$$\Delta C_j = \frac{C_0(1-f)^{n_0}\Delta K^{n_0}\left(1-\frac{\Delta H_{\mathrm{th}}}{\Delta K}\right)^{p_0}}{(1-R)^{n_0}\left(1-\frac{\Delta K}{(1-R)K_{\mathrm{c}}}\right)^{q_0}}\Delta N_j \tag{13}$$

The critical stress intensity factor determines the crack propagation termination activity. When $K_{\max} \geqslant K_{\mathrm{c}}$ or the net cross-section stress S_{n} is greater than the yield stress S_{Y}, failure occurs. Moreover, according to the modified Forman's equation, fatigue crack propagation is considered, and the critical value of variable stress intensity factor K determines the termination of fatigue crack propagation.

3 Conclusions

1) Through tensile tests at room temperature after annealing at 900, 1100, and 1300 °C, the microstructure, mechanical properties, and fracture process of rolled Mo-14%Re alloy are analyzed.

2) With the increase in annealing temperature, the Schmid factor of the Mo matrix phase and ReO_3 phase decreases gradually, the texture intensity increases rapidly, and the crystal orientation intensity of the polarography increases from 6.51 to 10.18.

3) The initial recrystallization temperature of the rolled Mo-14%Re is 1100 °C. At this time, the homogeneous precipitation of the earth-rich ReO_3 phase in the alloy leads to a uniform stress distribution during the tensile process, and the elongation after fracture reaches a maximum of 33.5%.

References

1 Feng B Q, Guo J L, Wang W *et al. China Molybdenum Industry*[J], 2013: 12

2 Hu P, Zhou Y H, Deng J *et al. J Alloys Compd*[J], 2018, 745: 532

3 Hu Ping, Song Rui, Wang Kuaishe *et al. Rare Metal Materials and Engineering*[J], 2017, 46(5): 1225

4 Xiang S, Yao Y, Wan Y *et al. Nutrients*[J], 2016, 12(8): 826

5 US Geological Survey. *Mineral Commodity Summaries 2011*[M]. US: Gedogical Survey, 2011

6 Amelunxen P, Wilmot J C, Easton C *et al. US Patent*[P], US20070780850, 2007

7 Que Z, Wei Z, Li X *et al*. *Journal of Materials & Technology*[J], 2022, 31(10): 203

8 Leichtfried G, Schneibel J H, Heilmaier M *et al. Metallurgical and Materials Transactions A*[J], 2006, 37(10): 2955

9 Davidson D L. *Journal of Applied Physics*[J], 1968, 39(12): 5768

10 Hu Ping, Wang Kuaishe, Yang Fan *et al. Rare Metal Materials and Engineering*[J], 2014, 43(7): 1722 (in Chinese)

11 Kang Xuanqi, Wang Kuaishe, Hu Ping *et al. Rare Metal Materials and Engineering*[J], 2015, 44(5): 1254 (in Chinese)

12 He Huancheng, Wang Kuaishe, Hu Ping *et al. Rare Metal Materials and Engineering*[J], 2014, 43(4): 964 (in Chinese)

13 Hu P, Hu B L, Wang K S *et al. Materials Science and Engineering A*[J], 2016, 678: 315

14 Leonard K J, Busby J T, Zinkle S J *et al. Journal of Nuclear Materials*[J], 2007, (3): 336

15 Leonhardt T, CarleN J C, Buck M *et al. Conference Proceedings*[M]. US: American Institute of Physics, 1999: 685

16 Agnew S R, Leonhardt T. *JOM*[J], 2003, 55(10): 25

17 Zhu G, Fang Z, Chen J *et al.* Hydrometallurgy[J], 1994, 94: 541

18 Golmakani M H, Khaki J V, Babakhani A *et al. Materials Chemistry and Physics*[J], 2017, 194: 9

19 Liu S. *International Journal of Refractory Metals & Hard Materials*[J], 1997, 15(4): 219

20 Sha L. *International Journal of Refractory Metals & Hard Materials*[J], 1999, 17(5): 381.

21 Han F T, Wang Z C, Jing C N *et al*. *Applied Mechanics & Materials*[J], 2013, 331: 551

22 Zhang J L, Li Zhong Kui, Fu Jie *et al. China Molybdenum Industry*[J], 2010, 34(5): 32

23 Wadsworth J, Nieh T G, Stephens J J *et al. Scripta Metallurgica*[J], 1986, 20(5): 637

24 Mannheim R L, Garin J L. *Journal of Materials Processing Technology*[J], 2003, 48(9): 1666

25 Garin J L, Mannheim R L. *Key Engineering Materials*[J], 2001, 189–191: 394

26 Busby J T, Leonard K J, Zinkle S J *et al. Journal of Nuclear Materials*[J], 2007, 366(3): 388

27 Haydock R. *Journal of Physics C Solid State Physics*[J], 1981, 14(26): 3807

28 Beck P A. *Interscience Publishers*[J], 1963, 112(6): 135

29 Liu Z, Li P, Xiong L *et al. Materials Science and Engineering A*[J], 2016, 680: 259

30 Galiyev A, Kaibyshev R, Gottstein G *et al. Acta Materialia*[J], 2001, 49(7): 1199

31 Zhong Q P. *Crack Studies*[M]. Beijing: Higher Education Press, 2014 (in Chinese)

32 Le A N, Zhang Y P, Gen Ye *et al. Hot Working Technology*[J]. 2011, 18(10): 23

33 Chen Y, Li J, Tang B *et al. Journal of Alloys and Compounds*[J], 2015, 618(5): 146

34 Yuan W J, Zhou F, Zhang Z L *et al. Materials Science & Engineering A*[J], 2013, 561: 183

35 Bridgman P W. *The Stress Distribution at the Neck of a Tension Specimen*[M], New York: Harvard University Press, 1964

36 Paris P, Erdogan F. *Journal of Basic Engineering*[J], 1963, 85(4): 528

37 Newman J. *A Fatigue Crack Growth Structural Anaysis Program*[R]. US: NASA, 1992

38 Kim J H, Lee S B. *Engineering Fracture Mechanics*[J], 2000, 66: 1

39 Tanaka K, Nakai Y, Yamashita M *et al. International Journal of Fracture*[J], 1981, 17(5): 519

轧制Mo-14%Re合金的显微组织和室温拉伸性能

何朝军[1,2]，胡　平[1,2]，邢海瑞[1,2]，杨　帆[1,2]，张向阳[1,2]，林小辉[3]，华兴江[1,2]，白　润[3]，张　文[3]，王快社[1,2]

(1. 西安建筑科技大学 冶金工程学院，陕西 西安 710055)

(2. 西安建筑科技大学 功能材料加工国家地方联合工程研究中心，陕西 西安 710055)

(3. 西北有色金属研究院，陕西 西安 710016)

摘　要：为了进一步了解轧制Mo-14%Re合金的显微组织和室温拉伸性能，采用扫描电镜（SEM）和高分辨电子背散射衍射（EBSD）研究了轧制Mo-14%Re合金的显微组织和断口形貌。采用Channel 5软件分析了轧制Mo-14%Re合金在不同退火温度下的组织演变。结果表明，随着退火温度的升高，Mo基体相和ReO_3相的施密特因子逐渐减小。织构强度迅速增加，极图上的晶体取向强度从6.51增加到10.18。轧制Mo-14%Re合金的初始再结晶发生在1100 ℃，在此退火温度下，合金中富稀土ReO_3相均匀析出，导致拉伸过程中应力分布均匀，Mo基体相和ReO_3相表现出明显的晶体取向，ReO_3相晶界主要为大角度晶界，使得断后伸长率达到最大值33.5%。拉伸断裂的韧窝数量最多且最大。此外，还研究了断裂过程中微孔的形成、聚集、生长和裂纹扩展。

关键词：Mo-14%Re合金；室温拉伸；初始再结晶；微观结构演化；裂纹扩展

作者简介：何朝军，男，1996年生，硕士生，西安建筑科技大学冶金工程学院，陕西 西安 710055，E-mail：2436242198@qq.com